Journal of Ceramic Processing Research. Vol. 26, No. 1, pp. 82~90 (2025)
(Received 30 September 2024, Received in revised form 15 December 2024, Accepted 3 January 2025)
https://doi.org/10.36410/jcpr.2025.26.1.82

J O U R N A L O F
Ceramic Processing Research

Growth of SiC nanostructures via mixed-source hydride vapor-phase epitaxy method

Suhyun Mun[a,#], Kyoung Hwa Kim[b,#], Seonwoo Park[a], Eunmin Kwon[a], Min Yang[a], Hyung Soo Ahn[a,*], Injun Jeon[c], Hunsoo Jeon[b], Jae Hak Lee[a,d], Kwanghee Jung[e], Won Jae Lee[e], Myeong-Cheol Shin[f] and Sang-Mo Koo[f]

[a]*Department of Nano-Semiconductor Engineering, National Korea Maritime and Ocean University, Busan 49112, Republic of Korea*
[b]*Power Semiconductor Commercialization Center, Busan Techno Park, Busan 46239, Republic of Korea*
[c]*Daegu Gyeongbuk Institute of Science & Technology, Division of Energy Technology, Daegu 42988, Republic of Korea*
[d]*LNBS Co., Ltd., Busan 48731, Republic of Korea*
[e]*Department of Advanced Materials Engineering, Dong-Eui University, Busan 47340, Republic of Korea*
[f]*Department of Electronic Materials Engineering, Kwangwoon University, Seoul 01897, Republic of Korea*

SiC nanostructures are stable without raw material loss even in high-temperature and extreme environments. Thus, they have applications in power semiconductors, optoelectronic devices, and secondary batteries. In this study, SiC nanostructures were grown via the mixed-source hydride vapor-phase epitaxy method with Si and graphite sources, and the growth mechanism was elucidated. The SiC nanostructures primarily grew between the SiC substrate and the graphite source, whereas carbon nanostructures grew on the surface of the graphite source. The properties of the SiC nanostructures grown in this study were characterized using field-emission scanning electron microscopy, energy dispersive spectroscopy, Raman spectroscopy, X-ray diffraction, and high-resolution transmission electron microscopy. The d-spacing between two adjacent lattice fringes was 0.25 nm, which is in good agreement with the interplanar spacing in the (111) or (102) plane directions of SiC. Moreover, the applicability of SiC nanostructures was evaluated by applying the material, which coexists with carbon nanostructures, as an anode in a lithium-ion battery.

Keywords: Mixed-source hydride vapor-phase epitaxy method, SiC nanostructures, Hexagonal SiC, Lithium-ion battery, Raman spectroscopy.

Introduction

SiC nanostructures have garnered significant research attention owing to their unique high-voltage and high-current characteristics [1-15]. The properties of SiC include a wide energy bandgap (2.3-3.3 eV), high critical electric field (2.0-4.0 MV/cm), and high thermal conductivity (3.2-4.9 W/cm·K). Thus, SiC nanostructures are crucial in high-temperature and high-power electronic device applications [16, 17]. Most SiC nanostructures are typically in the 3C-SiC form, and synthesizing 4H-SiC and 6H-SiC nanostructures remains a challenging task. 4H-SiC and 6H-SiC nanostructures have potential applications in high-temperature and high-power electronic devices owing to their high thermal stability, high breakdown voltage, and excellent thermal conductivity [18-22]. SiC nanostructures can maximize the advantages of these polytypes, and their excellent physical properties at the nanoscale suggest potential applications in various fields, such as electronic devices, energy storage devices, and optoelectronic devices.

Recently, anode materials that can replace graphite and help increase the capacity of lithium-ion batteries (LIBs) have been investigated [23-31]. Among anode materials, Si is one of the most promising next-generation LIB anode materials because it exhibits a theoretical capacity of 4200 mAh g^{-1}, which is more than 10 times higher than that of graphite (372 mAh g^{-1}) [32]. However, despite its high theoretical capacity, Si suffers from volume expansion of up to 420% during lithiation upon charging and discharging [33]. To overcome these problems, alternatives such as forming Si/C composites [24-28] and growing silicon into nanoparticles and utilizing them as anode materials have been examined [29-31]. For example, in a theoretical investigation, Wang et al. considered g-SiC_5 and g-SiC_2 as high-capacity anode materials for LIBs and found that these materials offer theoretical capacities of 1520 and 1286 mAh g^{-1}, respectively [34]. These results show that SiC nanostructures are promising alternative anode materials for LIBs. However, further research is required to achieve

[#]Equally contributed
[*]Corresponding author:
Tel : +82-10-8594-6302
E-mail: ahnhs@kmou.ac.kr

high yields and obtain high-quality SiC nanostructures.

The hydride vapor-phase epitaxy (HVPE) method offers a significant advantage over metal–organic chemical vapor deposition and molecular beam epitaxy methods: growth rates of several tens to hundreds of micrometers per hour can be achieved via HVPE, and thus, HVPE is considerably faster than other techniques [35-39]. In particular, the mixed-source HVPE method for growing SiC nanostructures is a relatively simple technique with the advantage of growth using the quantity control of the source materials in one graphite boat [40, 41]. Therefore, the growth of SiC nanostructures via the mixed-source HVPE method can be considered an innovative approach for enhancing SiC crystal yield. In this study, SiC nanostructures incorporating the characteristics of 6H-SiC and 4H-SiC were synthesized using Si and graphite sources, and the growth mechanism was analyzed. Furthermore, the application potential of SiC nanostructures was evaluated by fabricating LIBs with SiC nanostructures as the anode and examining the charge/discharge profile.

Experimental

Fig. 1 shows a schematic of the mixed-source HVPE apparatus used for growing SiC nanostructures. The mixed-source HVPE equipment comprises a furnace with three high-temperature zones (T ≈ 1200 °C) and a specially designed graphite boat placed within a quartz reactor tube. The sources—20 g of Ga, 20 g of Al, 20 g of graphite, and 30 g of Si—were mixed and placed in the graphite boat [42, 43]. Cylindrical graphite with an average diameter of 2 mm and a length of 8 mm was used as the graphite source. Small pieces of n-type Si substrates were used as the Si source. The high-purity Ga (7N) removed oxides and nitride films from the surface of Al and thereby, promoted the reaction between Al and HCl [44, 45]. The 4N metallic Al induced the formation of AlN nanostructures, and the grown AlN nanostructures adsorbed Si and C elements, resulting in the growth of SiC nanostructures [46]. HCl and NH_3 were used as reaction gases, and N_2 was used as the carrier gas. HCl, NH_3, and N_2 were flown into the quartz reactor tube through the inner quartz tube at flow rates of 200, 1000, and 5000 sccm, respectively. The SiC nanostructures were grown at a growth temperature of 1200 °C and a growth duration of 60 min. The SiC nanostructures were analyzed via field-emission scanning electron microscopy (FE-SEM; TESCAN MIRA3), energy dispersive spectroscopy (EDS; TESCAN MIRA3), Raman spectroscopy (Analytik Jena AG UniDRON), Cs-corrected high-resolution transmission electron microscopy (HRTEM; JEOL ARM200), and high-resolution X-ray diffraction (XRD; Rigaku SmartLab). For Raman spectroscopy, the grown nanostructures were attached to the carbon tape used in the FE-SEM measurements. The spectra were obtained using a 5 mW laser with a wavelength of 532 nm. The laser used in Raman spectroscopy had crossed polarization components, with a resolution of approximately 1 cm^{-1}, capable of detecting peak shifts as small as ~0.1 cm^{-1}. All measurement results were calibrated using the Rayleigh line as the zero Raman shift reference, and the cycle time was set to 5 s.

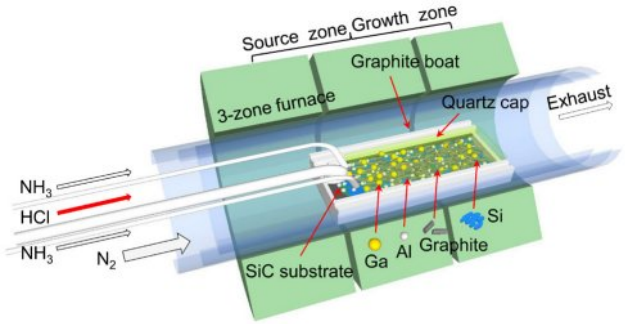

Fig. 1. Schematic of the mixed-source HVPE system used to grow SiC nanostructures.

Results and Discussion

Fig. 2(a) shows an optical image of the mixed-sources in the actual graphite boat. SiC nanostructures can grow on the SiC substrate when the SiC substrate is placed at the bottom of the graphite boat before introducing the sources. Thus, SiC nanostructures grew at the contact points between the SiC substrate (at the bottom) and the graphite source. Fig. 2(b) shows the changes in the surface of the graphite source after growth. A large number of nanostructures were formed on the surface (Fig. 2(c)). The

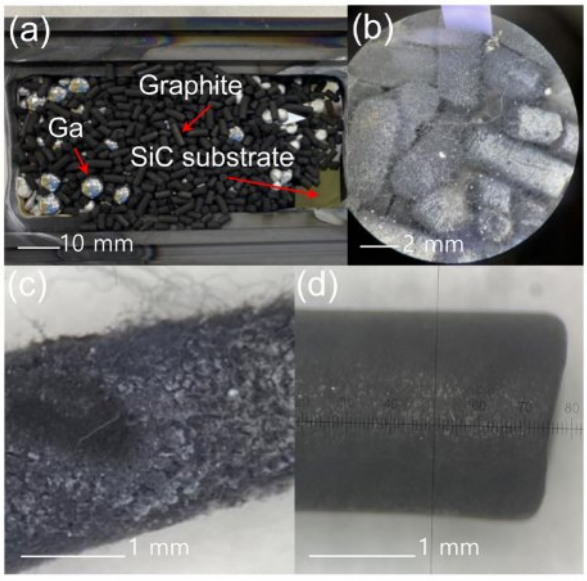

Fig. 2. (a) Image of the mixed-source inside the graphite boat used for growth. (b) Image of the graphite source after growth. (c) Enlarged image of the graphite source after growth. (d) Image of the graphite source before growth.

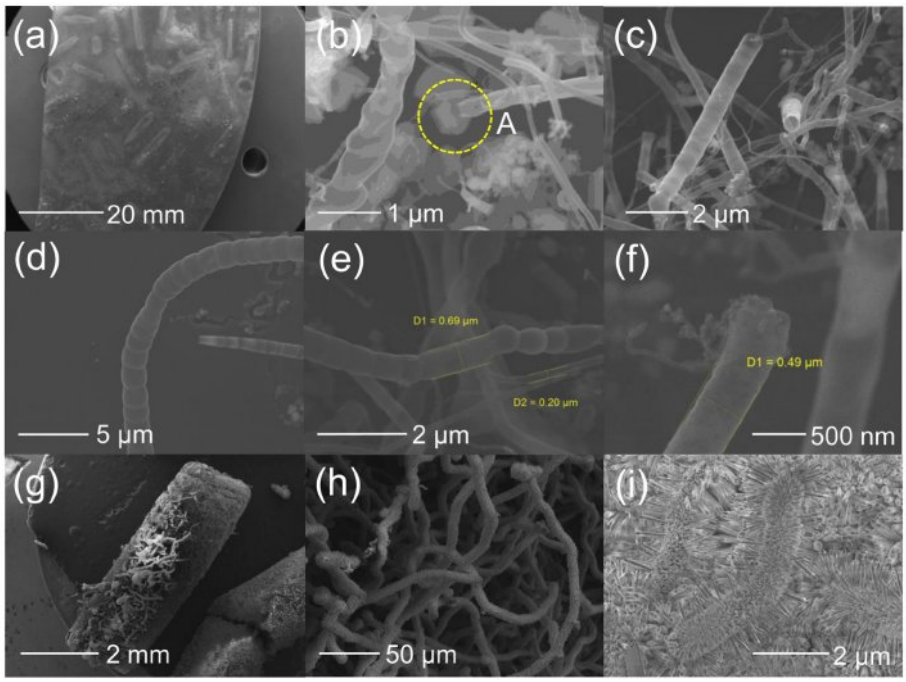

Fig. 3. (a) FE-SEM images of the surface of a SiC substrate placed on the bottom of a graphite boat. (b) Nanostructures grown on the SiC substrate. (c) Nanostructures in the form of a hollow tube. (d) Nanostructures with a typical bamboo-like shape. (e) Nanostructures with a diameter of approximately 200 to 700 nm. (f) Nanostructures with a diameter of approximately 500 nm. (g) FE-SEM image of the graphite surface after growth. (h) AlN-based nanostructures. (i) Growth of hairy caterpillar-like structures.

composition was similar to that of carbon nanostructures with a low Si elemental ratio. The surface of the graphite source before growth (Fig. 2(d)) was similar to that of a typical pencil lead. Fig. 3 shows the FE-SEM images of the grown SiC nanostructures. Fig. 3(a) shows the surface image of the SiC substrate that was placed at the bottom. The mark where the graphite was placed is clearly visible. Higher magnification images of the SiC substrate revealed that hexagonal seed structures were formed in some nanostructures, indicating the growth of nanostructures (Fig. 3(b) "A"). The nanostructures were shaped in the form of hollow tubes (Fig. 3(c)). Bamboo-like nanostructures with nodes were also observed (Fig. 3(d)) [47-54]. Compared to typical nanostructures, the diameter of the tubes was relatively large, ranging from 200 to 700 nm (Fig. 3(e)), with an average diameter of approximately 500 nm (Fig. 3(f)). The FE-SEM images shown in Fig. 3(g) indicate SiC nanostructure growth on the surface of the graphite source that was not in contact with the SiC substrate. Because the surface of the graphite source was directly exposed to HCl, NH_3 gas, AlCl, and $SiCl_n$, most nanostructures formed were of the AlN series (Fig. 3(h)). In particular, hairy caterpillar-like structures were observed, with nanostructures growing from their surfaces (Fig. 3(i)).

Fig. 4 shows the EDS results for the nanostructure shown in Fig. 3(b), wherein the compositional changes according to the position of the nanostructure are indicated. Fig. 4(a) shows the results for the hexagonal seed part. The elemental ratios related to C, Si, and

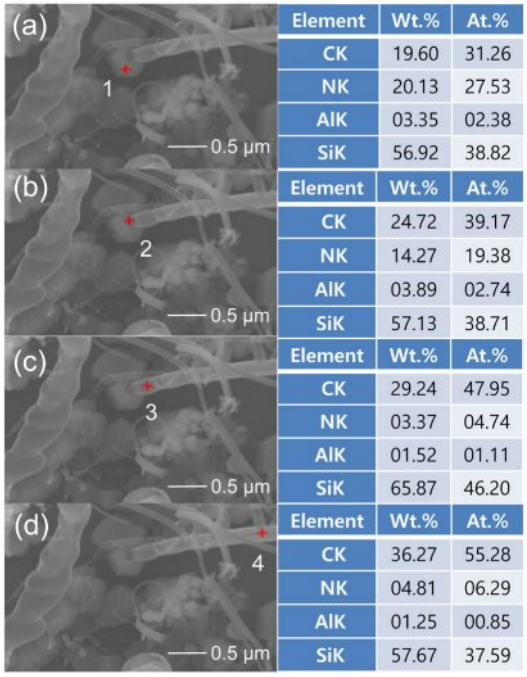

Element	Wt.%	At.%
CK	19.60	31.26
NK	20.13	27.53
AlK	03.35	02.38
SiK	56.92	38.82

Element	Wt.%	At.%
CK	24.72	39.17
NK	14.27	19.38
AlK	03.89	02.74
SiK	57.13	38.71

Element	Wt.%	At.%
CK	29.24	47.95
NK	03.37	04.74
AlK	01.52	01.11
SiK	65.87	46.20

Element	Wt.%	At.%
CK	36.27	55.28
NK	04.81	06.29
AlK	01.25	00.85
SiK	57.67	37.59

Fig. 4. EDS results for the nanostructures: (a) position "1," (b) position "2," (c) position "3," and (d) position "4."

AlN were 31.26, 38.82, and 29.91 at.%, respectively, indicating a similar distribution (Fig. 4(a) "1"). At the starting point of nanostructure growth (Fig. 4(b) "2"), the elemental ratios of C and Si increased to 39.17 and 38.71 at.%, respectively, whereas the elemental ratio related

to AlN decreased to 22.12 at.%. This indicates that the AlN nanostructures formed in the initial growth phase absorb Si and C and contribute to the growth of SiC nanostructures [44]. Consequently, as the nanostructures began to grow, C (47.95 at.%) and Si (46.20 at.%) were the major elements (Fig. 4(c) "3"). With continued nanostructure growth, the C content gradually increased to 55.28 at.%. This is attributed to the increasing activation of CCl_n formation over time from the graphite source in the mixed-source [55] (Fig. 4(d) "4").

Fig. 5(a) shows the variation in the elemental ratios according to the position of the nanostructure. As explained in the previous paragraph (Fig. 4), the increase in the elemental ratios of C and Si with continued nanostructure growth indicates the growth of SiC nanostructures. Fig. 5(b) shows the XRD 2 theta/omega results measured in the 2θ range of 20-80° for a sample placed on a glass jig. For graphite carbon (JCPDS file no: 26-1079), two diffraction peaks corresponding to the (003) and (101) lattice planes were observed at 26.4° and 43.3°, respectively. However, the observed diffraction peaks at 26.8° and 35.6° were distinct from the 33.6° peak corresponding to the (111) lattice plane of 3C-SiC (JCPDS file no: 75-0254). The peak at 26.8° corresponds to the (002) diffraction plane of hexagonal graphite (JCPDS file no: 41-1487), and the peak at 35.6° may be attributed to either the (004) lattice plane of 4H-SiC nanostructures (JCPDS file no: 22-1317) or the (102) lattice plane of 6H-SiC (JCPDS file no: 29-1128) [23, 49, 56-60]. Therefore, the grown nanostructures are deduced to be a composite of 4H-SiC or 6H-SiC

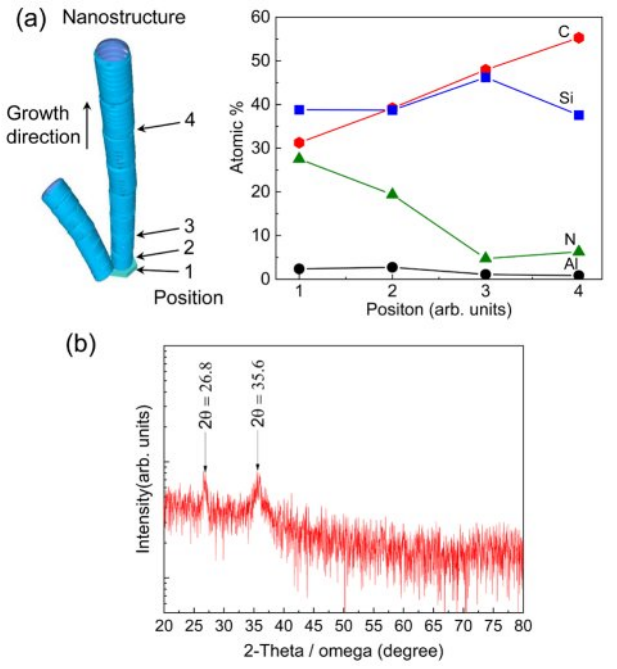

Fig. 5. (a) Variation in the proportion of each element as function of the position of the nanostructure. (b) XRD results for the nanostructures.

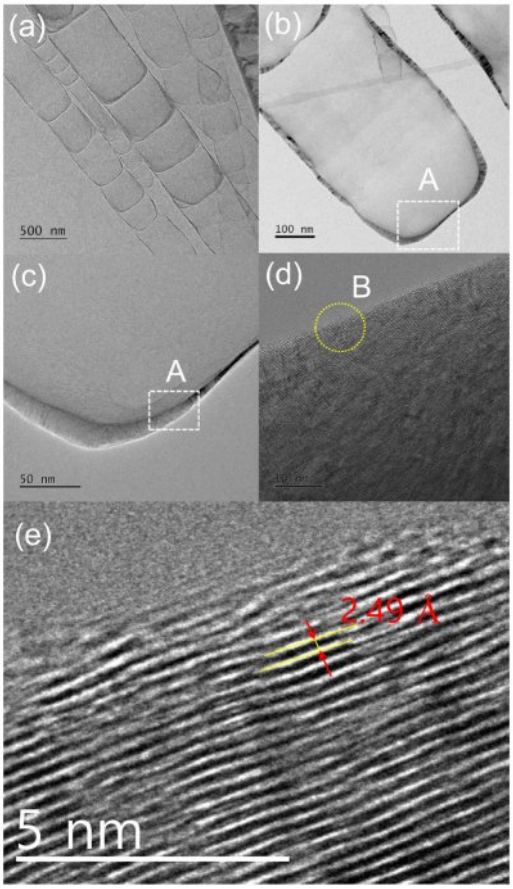

Fig. 6. HRTEM images of the SiC nanostructures. (a) HRTEM image of the ultrathin SiC nanostructures. (b) HRTEM image of ultrathin SiC nanowires with a diameter of 382 nm. (c) Enlarged image of the square marked "A" in (b). (d) HRTEM lattice image of square "A." (e) Enlarged image of the square marked "B" in (d).

nanostructures and carbon nanostructures.

Fig. 6 shows the HRTEM images of the grown nanostructures. Fig. 6(a) shows a typical HRTEM image of a SiC nanostructure. The edge of a SiC nanostructure with a width of 382 nm was measured (Fig. 6(b)). Fig. 6(c) shows an enlarged view of the region marked "A" in Fig. 6(b); the crystal structure can be observed in Fig. 6(d). Fig. 6(e) shows an enlarged image of the region marked "B" in Fig. 6(d): a periodic lattice structure was observed in the HRTEM lattice image. The d-spacing between two adjacent lattice fringes was 0.25 nm, which agrees well with the interplanar spacing along the (111) or (102) plane direction of SiC [23, 61-66]. These results confirm the growth of crystalline SiC nanostructures via the mixed-source HVPE method.

Fig. 7 shows the EDS results for the SiC nanostructures grown in different forms. Fig. 7(a) shows the EDS results for a SiC nanostructure with a diameter of 75 nm: the elemental ratios of C and Si were 43.33 and 53.69 at.%, respectively. Fig. 7(b) shows the EDS results for a SiC nanostructure with a diameter of 1300 nm: the elemental ratios of C and Si were 48.16 and 51.43 at.%,

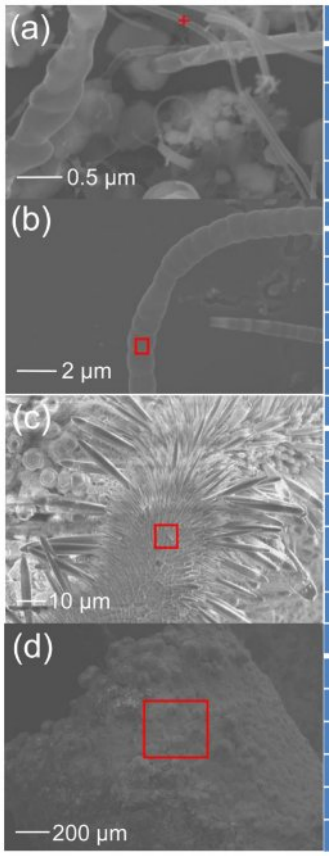

Element	Wt.%	At.%
CK	24.93	43.33
NK	01.10	01.63
AlK	01.74	01.35
SiK	72.23	53.69

Element	Wt.%	At.%
CK	28.44	48.16
NK	00.00	00.00
OK	00.00	00.00
GaL	00.00	00.00
AlK	00.54	00.41
SiK	71.02	51.43

Element	Wt.%	At.%
CK	06.35	12.26
NK	12.72	21.04
OK	00.22	00.31
GaL	01.42	00.47
AlK	13.99	12.01
SiK	65.31	53.90

Element	Wt.%	At.%
CK	01.28	02.45
NK	19.33	31.73
OK	01.40	02.01
GaL	04.11	01.35
AlK	58.26	49.65
SiK	15.63	12.80

Fig. 7. (a) EDS result for the 75 nm nanostructure. (b) EDS result for the 1300 nm nanostructure. (c) EDS result for the hairy caterpillar-like structure. (d) EDS result for the surface of graphite source after growth.

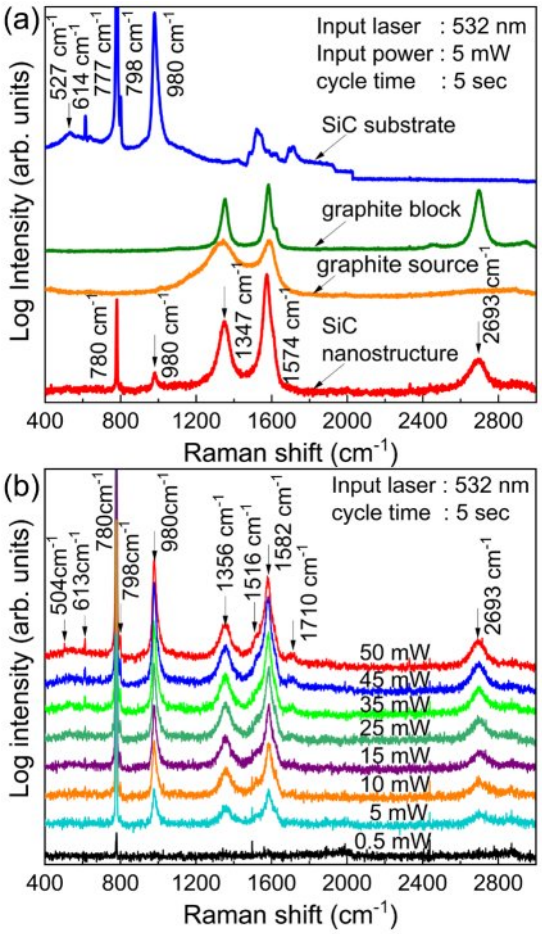

Fig. 8. Results of Raman measurement. (a) Raman results of various materials. (b) Raman measurement results for the SiC nanostructures according to incident laser power.

respectively. These results confirm the high stability of the SiC nanostructure with a near 50:50 ratio of C to Si [8, 20]. Fig. 7(c) shows the EDS results for the hairy caterpillar-like structure shown in Fig. 3(i): the elemental ratios of C, Si, and AlN were 12.26, 53.90, and 33.05 at.%, respectively. Fig. 7(d) presents the EDS results for the surface of the graphite source after growth: the elemental ratios of C and Si were low at 2.45 at.% and 12.80 at.%, respectively, whereas the elemental ratio of AlN was high at 81.38 at.%. This indicates that the AlN nanostructures from the mixed-source, along with the graphite source, contribute to the growth of SiC nanostructures by acting as an absorbent for the elements [46].

Fig. 8 shows the Raman spectroscopy results for the grown SiC nanostructures. Fig. 8(a) shows a comparison of the Raman spectra of the SiC substrate, graphite block, graphite source, and the grown SiC nanostructures. The SiC substrate exhibited modes at 527, 614 (LT; longitudinal-transverse), 777 (TO; transverse optical), 798 (TO), and 980 (LO; longitudinal optical) cm^{-1}, which are typical Raman peaks of bulk 4H-SiC crystals [67-72]. The graphite block and graphite source exhibited characteristic D and G peaks at 1354 and 1581 cm^{-1}, respectively [73-75]. Fig. 8(b) shows the Raman analysis results as a function of the incident laser power. The peaks for the SiC nanostructures were observed at 504, 613, 780, 798, 980, 1356, 1516, 1582, 1710, and 2693 cm^{-1}. For the bulk 6H-SiC, the Raman peaks at 767, 789, and 797 cm^{-1} were attributed to the three TO phonon modes and the peaks at 889 and 965 cm^{-1} were attributed to the two LO modes. Therefore, the peak observed at 504 cm^{-1} corresponds to the transverse acoustic (TA) mode of 6H-SiC, the peak at 613 cm^{-1} corresponds to the LT mode of 4H-SiC, the peak at 780 cm^{-1} corresponds to the TO mode of 4H-SiC, the peak at 798 cm^{-1} corresponds to the TO modes of both 6H-SiC and 4H-SiC, and the peak at 980 cm^{-1} corresponds to the LO mode of 4H-SiC. These results indicate that the Raman characteristics of the SiC nanostructures are distinct from those of the 4H-SiC substrate and bulk 6H-SiC [76-79]. In addition, the peaks at 1356, 1516, 1582, 1710, and 2693 cm^{-1} are primarily associated with SiC nanostructures and carbon structures, although distinguishing between them is challenging. Therefore, limiting the peaks related to SiC nanostructures to those below 1000 cm^{-1} is reasonable. Thus, both SiC

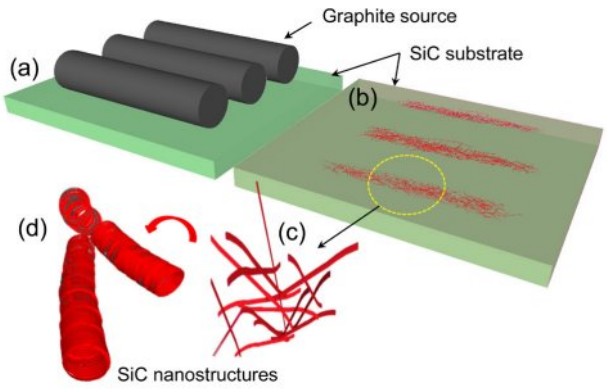

Fig. 9. Schematic of the growth of SiC nanostructures via the mixed-source HVPE method. (a) SiC substrate and graphite source layout diagram. (b) SiC substrate and grown SiC nanostructures. (c) SiC nanostructures. (d) Stable SiC nanostructures.

nanostructures and carbon nanostructures coexist in the sample.

Fig. 9 shows a schematic of the growth mechanism of SiC nanostructures obtained via mixed-source HVPE. The graphite source was placed on the SiC substrate (Fig. 9(a)). Fig. 9(b) shows that at 1200 °C, Ga, Al, graphite, and Si sources react with HCl gas to produce $GaCl_3$, AlCl, CCl_n, and $SiCl_n$; the reaction occurs at the interface between the SiC substrate and the graphite source. Here, Ga diffuses over the Al, graphite, and Si surfaces, leading to the formation of AlCl and the subsequent formation of AlN nanostructures [44, 45]. Moreover, unless Ga is used, Si does not readily react with HCl gas owing to the oxide and nitride layers on its surface. Thus, Ga facilitates the formation of CCl_n and $SiCl_n$. Consequently, a type of seed (shown in Fig. 4(a)) is formed, contributing to the growth of SiC nanostructures (Fig. 9(c)). Subsequently, CCl_n and $SiCl_n$ become essential components of the SiC

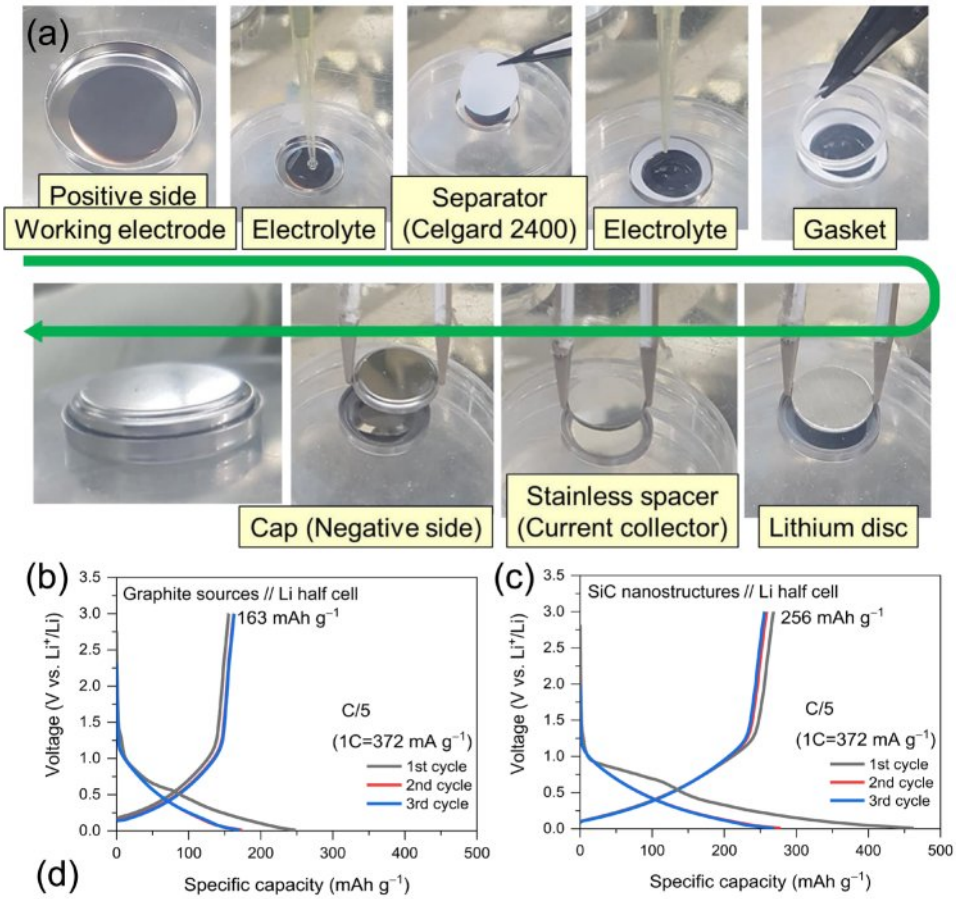

(d)

	1st Lithiation capacity (mAh g^{-1})	1st Delithiation capacity (mAh g^{-1})	1st Coulombic efficiency (%)
Graphite sources	248 mAh g^{-1}	155 mAh g^{-1}	63%
SiC nanostructures	462 mAh g^{-1}	268 mAh g^{-1}	58%

Fig. 10. (a) Fabrication of the LIB. Characteristics of LIB manufactured using the (b) graphite source used as a mixed-source and (c) nanostructures with coexisting SiC and carbon nanostructures. (d) Table showing a comparison of the characteristics.

nanostructures (Fig. 9(d)), leading to the growth of stable SiC nanostructures with a 50:50 ratio of C to Si [8, 20]. The same reaction occurs on the surface of the graphite source, resulting in the formation of hairy caterpillar-like structures with high Si content (Fig. 7(c)).

Fig. 10 shows the characteristics of an LIB fabricated using the grown SiC nanostructure. The cycle charge/discharge profiles obtained using commercial graphite, graphite source, and materials containing both SiC nanostructure and carbon nanostructure as anode active materials in LIB were compared. Fig. 10(a) shows the LIB fabrication process. The SiC nanostructures were pulverized using a ball mill. The pulverized SiC nanostructure powder was used as the active material for the anode of the secondary battery. The active material was mixed with a conductive agent (carbon black) and a binder to form a composite. The weight ratio (wt%) of the SiC nanostructure powder, carbon black, and binder was set to 80:10:10, and the mixture was homogenized using a ball mill for 10-12 h. It is estimated that the active material carbon black ratio of 80 contains approximately 10% of SiC nanostructure. Carboxymethyl cellulose dissolved in distilled water at a concentration of 1.0-1.5 wt.% was used as the binder. The resulting composite was then utilized to fabricate the anode. The composite was coated onto a copper foil attached to a flat glass plate using a doctor blade apparatus. The coating thickness was set to 25 μm, and the coated anode material was dried at 80 °C for 10 h. The final anode was fabricated by punching the anode material to the required size. Subsequently, a coin-type LIB (coin cell) was assembled using the fabricated anode. The structure of the coin cell was in accordance with the CR2032 coin cell standard, which specifies a diameter of 20 mm and a thickness of 3.2 mm. Disk electrodes with diameters of 16 and 14 mm were used as the anode and cathode, respectively. The active material in the 14 mm diameter region was used for charge storage. A small amount of electrolyte was applied on the fabricated SiC nanostructure-based anode. The electrolyte consisted of either 1 M $LiPF_6$ EC/DEC (1:1, v/v) + 10 wt.% FEC or 1 M $LiPF_6$ EC/DEC (1:1, v/v) + 1 wt.% VC. A monolayer polypropylene separator (Celgard 2400) was placed on the anode, and a gasket was attached. The cathode, composed of lithium foil (D14 mm T0.5), and a stainless-steel disk, serving as the current collector, were then placed on the top. Additional electrolyte was added, and a spring was inserted to provide structural cushioning. The top cover was placed, and the cell was pressed using a crimping tool to complete the assembly. The assembled coin cell was manufactured in an argon-filled glovebox to prevent contamination, and the cell was allowed to soak in the electrolyte for 12 h to ensure adequate impregnation. Fig. 10(b) shows the charge/discharge characteristics for the initial 3 cycles for the graphite sources. The graphite source used in this study has extremely low capacities of 248 and 155 mAh g^{-1} during lithiation and delithiation, respectively. The lithiation and delithiation capacities obtained using the grown SiC nanostructure were 462 mAh g^{-1} and 268 mAh g^{-1}, respectively, and the first-order Coulombic efficiency was 58 % (Fig. 10(c)). The SiC nanostructure-based anode resulted in the highest lithiation capacity of 462 mAh g^{-1}. Fig. 10(d) shows a comparison of the charge/discharge characteristics of two samples. The results for the grown SiC nanostructures in the last column of the table show a profile that is significantly different from that of common graphite [80-84]. Therefore, SiC nanostructures and carbon nanostructures coexist in the nanostructures used to fabricate the LIB in this study, suggesting that they are likely to be carbon materials other than pure graphite. Increasing the ratio of SiC nanostructures in the active material carbon black is expected to lead to different results. These aspects will be further investigated in future work.

Conclusions

Stable SiC nanostructures were successfully grown between the SiC substrate and the graphite source via the mixed-source HVPE method. The grown nanostructures were confirmed to be a mixture of SiC nanostructures and carbon nanostructures. The SiC nanostructures primarily grew between the SiC substrate and the graphite source, whereas the carbon nanostructures grew on the surface of the graphite source. The grown SiC nanostructures were stable and large, with a C to Si composition ratio of approximately 50:50. XRD, HRTEM, and Raman spectroscopy results indicated the presence of 4H-SiC and 6H-SiC structures, as well as carbon nanostructures. The grown nanostructures were used as an anode material for LIB, and the observed characteristics were different from those of common graphite. Thus, the growth of SiC nanostructures via the HVPE method is feasible. SiC nanostructures grown via the mixed-source HVPE method are expected to be an innovative example in the field of semiconductor growth.

Acknowledgments

This work was supported by the Korea Evaluation Institute of Industrial Technology (KEIT) grant funded by the Korean government in 2022 (MOTIE) (RS-2022-00154720, Technology Innovation Program Development of next-generation power semiconductor based on Si-on-SiC structure). This work was also supported by a Korea Institute for Advancement of Technology (KIAT) grant funded by the Korea Government in 2021 (MOTIE) (P0012451, The Competency Development Program for Industry Specialist).

References

1. C.H. Park, B. Cheong, K. Lee, and K.J. Chang, Phys.

Rev. B 49[7] (1994) 4485-4493.
2. C. Persson and U. Lindefelt, J. Appl. Phys. 82[11] (1997) 5496-5508.
3. X. Sun, C. Li, W. Wong, N. Wong, C. Lee, S. Lee, and B. Teo, J. Am. Chem. Soc. 124[48] (2002) 14464-14471.
4. A.T. Mulatu, K.N. Nigussa, and L.D. Deja, Materialia 20 (2021) 101257.
5. K. Kamaras, M.E. Itkis, H. Hu, B. Zhao, and R.C. Haddon, Science 301[5639] (2003) 1501.
6. C. Vatankhah and H.A. Badehian, Solid State Commun. 344 (2022) 114672.
7. C. Vatankhah and H.A. Badehian, Optik 237 (2021) 166740.
8. M. Luo, Y.H. Shen, and T.L. Yin, Optik 130 (2017) 589-593.
9. M. Li, L. Jiang, Y. Peng, T. Wang, T. Xiao, P. Xiang, and X. Tan, Optik 176 (2019) 401-409.
10. K. Kefif, Y. Bouizem, A. Belfedal, J.D. Sib, D. Benlakehal, and L. Chahed, Optik 154 (2018) 459-466.
11. M.D. Mohammadi, I.H. Salih, and H.Y. Abdullah, Mol. Simul. 46[17] (2020) 1405-1416.
12. S. Chabi and K. Kadel, Nanomaterials 10[11] (2020) 2226.
13. G. Liu, B.R. Tuttle, and S. Dhar, Appl. Phys. Rev. 2[2] (2015) 021307.
14. A.K. Ray and M.N. Huda, J. Comput. Theor. Nanosci. 3[3] (2006) 315-341.
15. A. Mavrandonakis, G.E. Froudakis, M. Schnell, and M. Mühlhäuser, Nano Lett. 3[11] (2003) 1481-1484.
16. X. She, A.Q. Huang, Ó. Lucía, and B. Ozpineci, IEEE Trans. Ind. Electron. 64[10] (2017) 8193-8205.
17. M. Östling, R. Ghandi, and C. Zetterling, Proc. 2011 IEEE 23rd Int. Symp. Power Semiconductor Devices and ICs, San Diego, CA, USA, 23-26 May 2011, p. 10.
18. G. Wei, W. Qin, G. Wang, J. Sun, J. Lin, R. Kim, D. Zhang, and K. Zheng, J. Phys. D: Appl. Phys. 41[23] (2008) 235102.
19. W.J. Choyke, Mater. Res. Bull. 4 (1969) S141.
20. A.A. Lebedev, Semicond. Sci. Technol. 21[6] (2006) R17-R34.
21. R. Han, X. Xu, X. Hu, N. Yu, J. Wang, Y. Tian, and W. Huang, Opt. Mater. 23[1-2] (2003) 415.
22. J. Kim, F. Rena, and S.J. Peartonb, J. Ceram. Process. Res. 7[3] (2006) 239.
23. J.-K. Lee and J.-R. Yoon, J. Ceram. Process. Res. 21[5] (2020) 533.
24. C.K. Chan, R.N. Patel, M.J. O'Connell, B.A. Korgel, and Y. Cui, ACS Nano 4[3] (2010) 1443-1450.
25. J. Shu, H. Li, R. Yang, Y. Shi, and X. Huang, Electrochem. Commun. 8[1] (2006) 51-54.
26. L.-F. Cui, Y. Yang, C.-M. Hsu, and Y. Cui, Nano Lett. 9[9] (2009) 3370-3374.
27. I.-J. Shon, J. Ceram. Process. Res. 17[11] (2016) 1171.
28. X. He, A. Tang, Y. Li, Y. Zhang, W. Chen, and S. Huang, Surf. Sci. 563 (2021) 150269.
29. B.M. Bang, H. Kim, J.-P. Lee, J. Cho, and S. Park, Energy Environ. Sci. 4[9] (2011) 3395.
30. H. Li, X. Huang, L. Chen, Z. Wu, and Y. Liang, Electrochem. Solid-State Lett. 2[11] (1999) 547.
31. H. Li, L. Shi, Q. Wang, L. Chen, and X. Huang, Solid State Ion. 148[3-4] (2002) 247-258.
32. R.A. Huggins, J. Power Sources 81-82 (1999) 13-19.
33. H. Wu and Y. Cui, Nano Today 7[5] (2012) 414-429.
34. H. Wang, M. Wu, X. Lei, Z. Tian, B. Xu, K. Huang, and C. Ouyang, Nano Energy 49 (2018) 67-76.
35. J.J. Wierer Jr, A. David, and M.M. Megens, Nat. Photon. 3[3] (2009) 163-169.
36. P.R. Tavernier, E.V. Etzkorn, Y. Wang, and D.R. Clarke, Appl. Phys. Lett. 77[12] (2000) 1804-1806.
37. T. Paskova, E.M. Goldys, R. Yakimova, E.B. Svedberg, A. Henry, and B. Monemar, J. Cryst. Growth 208[1-4] (2000) 18.
38. H.S. Ahn, K.H. Kim, M. Yang, J.Y. Yi, H.J. Lee, J.H. Chang, H.S. Kim, S.W. Kim, S.C. Lee, Y. Honda, M. Yamaguchi, and N. Sawaki, Phys. Stat. Sol. (a) 202[6] (2005) 1048-1052.
39. G.S. Lee, C. Lee, H. Jeon, C.Lee, S.G. Bae, H.S. Ahn, M. Yang, S.N. Yi, Y.M. Yu, J.H. Lee, Y. Honda, N. Sawaki, and S.W. Kim, Jpn. J. Appl. Phys. 55 (2016) 05FC02.
40. H. Jeon, I. Jeon, G.S. Lee, S.G. Bae, H.S. Ahn, M. Yang, S.N. Yi, Y.M. Yu, Y. Honda, N. Sawaki, and S.W. Kim, Jpn. J. Appl. Phys. 56 (2017) 01AD07.
41. S.G. Bae, I. Jeon, H. Jeon, K.H. Kim, M. Yang, S.N. Yi, J.H. Lee, H.S. Ahn, Y.M. Yu, N. Sawaki, and S.W. Kim, Jpn. J. Appl. Phys. 57 (2018) 01AD03.
42. H.S. Ahn, S.W. Kim, G.S. Lee, K.H. Kim, J.H. Lee, D.H. Ha, Y.T. Chun, and S. Ryu, Semicond. Sci. Technol. 36[9] (2021) 095023.
43. S. Park, S. Mun, K.H. Kim, M. Yang, Y.T. Chun, S.N. Yi, H.S. Ahn, J.H. Lee, Y.S. Jang, W.J. Lee, M.C. Shin, and S.M. Koo, J. Korean Phys. Soc. 84[3] (2024) 198-207.
44. O. Kovalenkov, V. Soukhoveev, V. Ivantsov, A. Usikov, and V. Dmitriev, J. Cryst. Growth 281[1] (2005) 87-92.
45. Y. Kumagai, T. Yamane, and A. Koukitu, J. Cryst. Growth 281[1] (2005) 62-67.
46. K.H. Kim, G.S. Lee, H.S. Ahn, J.H. Lee, J. Kim, Y.T. Chun, M. Yang, S.N. Yi, S. Hwang, and S. Kim, Semicond. Sci. Technol. 37[4] (2022) 045016.
47. A. Ashok, A. Kumar, J. Ponraj, and S.A. Mansour, Carbon 170 (2020) 452.
48. W. Yang, X. Liu, X. Yue, J. Jia, and S. Guo, J. Am. Chem. Soc. 137[4] (2015) 1436-1439.
49. Z.W. Tong, Y.F. Yuan, S.M. Yin, B.X. Wang, S.Y. Guo, and C.L. Mo, Mater. Lett. 311 (2022) 131587.
50. M. Lin, J.P.Y. Tan, C. Boothroyd, K.P. Loh, E.S. Tok, and Y. Foo, Nano Lett. 7[8] (2007) 2234-2238.
51. S. Iijima, Nature 354 (1991) 56-58.
52. J. Kong, H.T. Soh, A.M. Cassell, C.F. Quate, and H. Dai, Nature 395 (1998) 878-881.
53. Z.F. Ren, Z.P. Huang, J.W. Xu, J.H. Wang, P. Bush, M.P. Siegal, and P.N. Provencio, Science 282[5391] (1998) 1105-1107.
54. T. Katayama, H. Araki, and K. Yoshino, J. Appl. Phys. 91[10] (2002) 6675-6678.
55. Z.J. Pan and R.T. Yang, J. Catalysis 123[1] (1990) 206-214.
56. T. Taguchia, N. Igawa, H. Yamamoto, S. Shamoto, and S. Jitsukawa, Physica E 28[4] (2005) 431-438.
57. X.K. Li, L. Liu, Y.X. Zhang, S.D. Shen, S. Ge, and L.C. Ling, Carbon 39[2] (2001) 159-165.
58. J. Patel, C. Balasubramanian, C. Sasmal, and A. Satyaprasad, Physica E 103 (2018) 377-382.
59. H.X. Zhang, P.X. Feng, V. Makarov, B.R. Weiner, and G. Morell, Mater. Res. Bull. 44[1] (2009) 184-188.
60. L. Li, Y. Chu, H. Li, L. Qi, and Q. Fu, Ceram. Int. 40[3] (2014) 4455-4460.
61. Y. Zhang, X. Han, K. Zheng, Z. Zhang, X. Zhang, J. Fu, Y. Ji, Y. Hao, X. Guo, and Z.L. Wang, Adv. Funct. Mater. 17[17] (2007) 3435-3440.
62. D. Wang, D. Xu, Q. Wang, Y. Hao, G. Jin, X. Guo, and

K.N. Tu, Nanotechnology 19[21] (2008) 215602.
63. X.D. Han, Y.F. Zhang, K. Zheng, X.N. Zhang, Z. Zhang, Y.J. Hao, X.Y. Guo, J. Yuan, and Z.L. Wang, Nano Lett. 7[2] (2007) 452-457.
64. H. Kohno and H. Yoshida, Physica B 376-377 (2006) 890.
65. W. Zhou, X. Liu, and Y. Zhang, Appl. Phys. Lett. 89[22] (2006) 223124.
66. Q. Lu, J. Hu, K. Tang, Y. Qian, G. Zhou, X. Liu, and J. Zhu, Appl. Phys. Lett. 75[4] (1999) 507-509.
67. K.F. Domke and B. Pettinger, J. Raman Spectrosc. 40[10] (2009) 1427-1433.
68. M. Bechelany, A. Brioude, D. Cornu, G. Ferro, and P. Miele, Adv. Funct. Mater. 17[6] (2007) 939-943.
69. M. Mastellone, A. Bellucci, M. Girolami, R.M. Montereali, S. Orlando, R. Polini, V. Serpente, E. Sani, V. Valentini, M.A. Vincenti, and D.M. Trucchi, Opt. Mater. 107 (2020) 109967.
70. J. Zhu, J. Jia, F. Kwong, and D.H.L. Ng, Diamond Relat. Mater. 33 (2013) 5-11.
71. H. Jian, M. Dayan, and X. Kewei, Rare Met. Mater. Eng. 44[11] (2015) 2692-2697.
72. S. Nakashima and H. Harima, Phys. Stat. Sol. (a) 162[1] (1997) 9.
73. A.C. Ferrari, Solid State Commun. 143[1-2] (2007) 47.
74. R.P. Vidano, D.B. Fischbach, L.J. Willis, and T.M. Loehr, Solid State Commun. 39[2] (1981) 341-344.
75. I. Pocsik, M. Hundhausen, M. Koos, and L. Ley, J. Non-Cryst. Solids 227-230 (1998) 1083.
76. S.G. Sundaresan, A.V. Davydov, M.D. Vaudin, I. Levin, J.E. Maslar, Y. Tian, and M.V. Rao, Chem. Mater. 19[23] (2007) 5531-5537.
77. D.W. Feldman, J.H. Parker, W.J. Choyke, and L. Patrick, Phys. Rev. 173[3] (1968) 787-793.
78. H.Y. Kim, S.Y. Bae, N.S. Kim, and J. Park, Chem. Commun. 20 (2003) 2634.
79. S. Zhang, B. Zhu, F. Huang, Y. Yan, E. Shang, S. Fan, and W. Han, Solid State Commun. 111[11] (1999) 647-651.
80. I. Jeon, D. Yang, D. Yadav, J. Seo, H. Zhang, L. Yin, H.S. Ahn, and C. Cho, Electrochim. Acta 439 (2023) 141730.
81. B.G. Kim, W.H. Shin, S.Y. Lim, B.S. Kong, and J.W. Choi, J. Electrochem. Sci. Technol. 3[3] (2012) 116.
82. H.R. Byon, S.W. Lee, S. Chen, P.T. Hammond, and Y. Shao-Horn, Carbon 49[2] (2011) 457-467.
83. I. Jeon, J.H. Hwang, T.G. Kim, L. Yin, H.W. Lee, J.P. Kim, H.S. Ahn, and C.-R. Cho, J. Ceram. Process. Res. 22[2] (2021) 192.
84. C. Chen, X.C. Han, H.H. Shen, Y.Q. Tan, H.B. Zhang, Y. Qin, and S.M. Peng, Ceram. Int. 46[14] (2020) 23173-23179.